RSC Advances

PAPER

View Article Online
View Journal | View Issue

Cite this: *RSC Adv.*, 2025, **15**, 51100

Modulation of electronic and magnetic properties of defective and TM-doped Al_2SSe Janus monolayer (TM = Mn and Fe) through hole and electron doping

Nguyen Thi Han, [a] Chu Viet Ha, [b] Nguyen Thanh Son,[c] J. Guerrero-Sanchez[d] and D. M. Hoat *[ef]

Effective manipulation of electronic and magnetic properties plays a key role in designing practical applications of materials. In this work, the magnetism engineering in Al_2SSe monolayers is studied by creating pair Al (pVa) vacancies and doping with a pair of TM transition metals (pTM = Mn and Fe). Further, electronic and magnetic properties are modulated through hole and electron doping. The pristine Al_2SSe monolayer is intrinsically nonmagnetic, exhibiting an indirect gap of 2.04 eV. The creation of pVa-type defects induces half-metallicity, in-plane magnetic anisotropy (IMA), and an overall magnetic moment of 2.00 μ_B. In this case, first neighbor Se atoms and second neighbor Al atoms from defect sites primarily originate the system magnetic moment. The magnetism of the pVa@mo system can be significantly enhanced by electron doping that increases the magnetic moment and strengthens the IMA. Significant monolayer magnetization is also achieved by pTM doping, where impurities produce mainly magnetic properties. Paired Mn atoms show antiparallel spin alignment to form the ferrimagnetic (FiM) state of the pMn@mo system, which becomes weaker with electron doping. Meanwhile, the ferromagnetic (FM) state is stable in the pFe@mo system with parallel spin orientation of Fe impurities, which becomes much stronger with electron doping. Herein, a high Curie temperature of 972.40 K is obtained for the pFe@mo system, which increases considerably by electron doping. In addition, the electronic properties and magnetic anisotropy can be effectively controlled by varying carrier concentration. Our findings solidly pave the way to make artificially two-dimensional magnetic materials from the Janus monolayer Al_2SSe, where further hole and electron doping can modulate the electronic and magnetic properties of the defective and doped systems towards selective spintronic applications.

Received 27th November 2025
Accepted 14th December 2025

DOI: 10.1039/d5ra09165a

rsc.li/rsc-advances

I. Introduction

It is well known that nanomaterials – with at least one of their dimensions in the nanometre scale – exhibit enhanced physical and chemical properties in comparison with their bulk counterparts.[1,2] When restricting only one dimension, two-dimensional (2D) materials will be formed with novel properties originating from quantum confinement effects and their high specific surface area.[3,4] Graphene is the first atom-thick material with macroscopic lateral dimensions to be isolated (from graphite).[5] So far, extensive experimental and theoretical studies have demonstrated extraordinary properties of graphene and its derivatives, endowing promise for diverse applications, such as high-speed electronics and optoelectronics,[6,7] energy generation and storage,[8,9] gas sensing,[10,11] catalysis,[12,13] bimedicine,[14,15] and environmental remediation,[16,17] among others. The success of graphene has created renewed interest in 2D materials that can be isolated from their layered bulk structures facilitated by weak van der Waals interactions[18,19] or can be grown from precursors using advanced techniques such as chemical vapor deposition (CVD)[20,21] and molecular beam epitaxy (MBE).[22,23] In addition, modern quantum chemistry with accurate calculations – facilitated by the powerful high-performance computer (HPC) systems – has allowed the prediction of stability and physicochemical properties of materials. Consequently, a large variety of 2D materials beyond graphene with different allotropes and chemical compositions

[a]*Department of Basic Science, Hung Yen University of Technology and Education, Hung Yen, Vietnam*

[b]*Faculty of Physics, TNU-University of Education, Thai Nguyen, 250000, Vietnam*

[c]*Center of Scientific Research and Application, Lac Hong University, No. 10 Huynh Van Nghe Str, Tran Bien Ward, Dong Nai Province, Vietnam*

[d]*Universidad Nacional Autónoma de México, Centro de Nanociencias y Nanotecnología, Apartado Postal 14, Ensenada, Baja California, Código Postal 22800, Mexico*

[e]*Institute of Theoretical and Applied Research, Duy Tan University, Ha Noi 100000, Vietnam. E-mail: dominhhoat@duytan.edu.vn*

[f]*School of Engineering and Technology, Duy Tan University, Da Nang 550000, Vietnam*

have been explored experimentally and theoretically. This family displays diverse intriguing properties, including metallic nature,[24,25] semimetal,[26,27] semiconductor,[28,29] insulator,[30,31] and topological insulator.[32,33]

On the other hand, the layer-structured III-monochalcogenide semiconductors have attracted great attention due to their promise for optoelectronics,[34] photovoltaics,[35] terahertz generation,[36] and nonlinear optical.[37] Reducing one dimension, they form one of the most important groups of 2D semiconductor materials with tunable band gap, high carrier mobility, high charge density, and efficient light absorption.[38,39] These characteristics endow III-monochalcogenide semiconductors high-performance device applications in some fields, including electronic, optics, and optoelectronics. Besides, researchers have demonstrated the magnetization of these 2D III–VI materials induced by lattice defects and doping with transition metals, opening new magnetic functionalities.[40–43] In addition, Meng *et al.*[44] have revealed the ferromagnetism and half-metallicity in GaO and InO monolayers induced by hole doping. Similar effects of hole doping have been also found for Janus M_2SO (M = Ga, In, and Tl) monolayers.[45]

It is important mentioning that most of the studies explore those Ga- and In-based materials, meanwhile Al-monochalcogenides have received much less attention despite they have quite similar electronic profiles compared to other III–VI group members.[46,47] In addition, Al_2SSe Janus monolayer has been also predicted using first-principles calculations.[48–51] Results show prospective optoelectronic, thermoelectric, and piezoelectric properties of this Janus structure. To the best of our knowledge, the magnetism engineering in Al_2SSe monolayer has not been investigated well, so far. In this work, we propose the creation of pair Al vacancies and doping with pair transition metals (TMs = Mn and Fe) to induce feature-rich magnetic and electronic properties in Al_2SSe Janus monolayer. Further, hole and electron doping is also proposed to control the magnetic phase and anisotropy of the defective and doped systems, which is crucial for their selective spintronic applications. Our study may provide good theoretical guidance for experiments, where doping process can be realized by CVD method with transition metal precursors[52] or creating pair Al vacancies followed by filling with transition metals.[53]

II. Computational details

Within the framework of density functional theory (DFT),[54] the projector-augmented wave (PAW) method and Perdew–Burke–Ernzerhof-parameterized generalized gradient approximation (GGA-PBE)[55] are employed to investigate the electronic and magnetic properties of pristine, defective, and doped Al_2SSe Janus monolayer. It is worth mentioning that PBE functional generally underestimates the electronic band gap of materials. Therefore, some alternative methods as self-interactions corrections and hybrid functional have been proposed to give more accurate results.[56–58] However, because of its low computational cost and capability of describing well the band structure profile, PBE functional is chosen in this work. All calculations are performed with the help of Vienna *ab initio* simulation package (VASP).[59,60] Since 3d electrons of Mn and Fe transition metals may have strong correlation, DFT+U by Dudarev *et al.*[61] is also adopted in calculations to treat properly the correlation effects using an effective Hubbard parameter of U_{eff} = 4 eV that has been commonly employed.[62] To consider the effects of weak van der Waals interactions, DFT-D3 method is chosen.[63] Cutoff energy of 500 eV is set when expanding the plane-wave basis set. All the structural models are relaxed until the residual forces on individual constituent atom satisfy the convergence criterion of 1×10^{-2} eV Å^{-1}. The self-consistency criterion of energy is set to 1×10^{-6} eV. *k*-Point grids are generated using Monkhorst–Pack method.[64] Herein a *k*-point mesh of $20 \times 20 \times 1$ is generated for pristine monolayer modeled by an unit cell. In all cases, the crystal structures contain a vacuum region along *z*-axis perpendicular to the monolayer plane (*xy*-plane), where a vacuum thickness more than 16 Å can guarantee negligible interactions between monolayer images.

In order to study pair Al vacancies (pVa) and pair-transition-metals (pTM = pMn and pFe) doping, a $4 \times 4 \times 1$ supercell of Al_2SSe monolayer is generated, for which the Brillouin zone integration is performed with a $4 \times 4 \times 1$ *k*-point mesh. Formation energy E_f of the defective (pVa@mo) and doped (pMn@mo and pFe@mo) systems is calculated using following expression:

$$E_f = \frac{E(\mathrm{D@mo}) - E(\mathrm{mo}) + 2\mu_{Al} - 2\mu_{TM}}{2} \quad (1)$$

where, E(D@mo) (D = pVa, pMn, and pFe) and E(mo) are total energy of the defective/doped and pristine Al_2SSe systems, respectively; μ_{Al} and μ_{TM} denote chemical potential of Al and TM atoms calculated from their bulk phase, respectively. Then, cohesive energy E_c of D@mo systems is estimated as follows:

$$E_c = \frac{E(\mathrm{D@mo}) - n_{Al}E(\mathrm{Al}) - n_{TM}E(\mathrm{TM}) - n_S E(\mathrm{S}) - n_{Se}E(\mathrm{Se})}{n_{Al} + n_{TM} + n_S + n_{Se}} \quad (2)$$

herein, E(X) is energy of single X atom and n_X refers to the number of X (X = Al, TM, S, Se) atoms in the defective/doped systems.

For the magnetic systems, the magnetic anisotropy is essential to suggest their applications. This property is studied using magnetic anisotropy energy (MAE) that is calculated through the energy difference as follows:

$$\mathrm{MAE} = E^{\parallel} - E^{\perp} \quad (3)$$

where, total system energies $E^{\parallel}$ and $E^{\perp}$ are calculated when the easy magnetization axis is set along [100] parallel to and [001] perpendicular to the monolayer plane, respectively.

III. Results and discussion

A. Structural and electronic properties of pristine Al_2SSe Janus monolayer

Fig. 1a shows the optimized $4 \times 4 \times 1$ supercell of Al_2SSe Janus monolayer, whose unit cell contains one formula unit. The structure displays the atomic stacking S–Al1–Al2–Se, where Al1

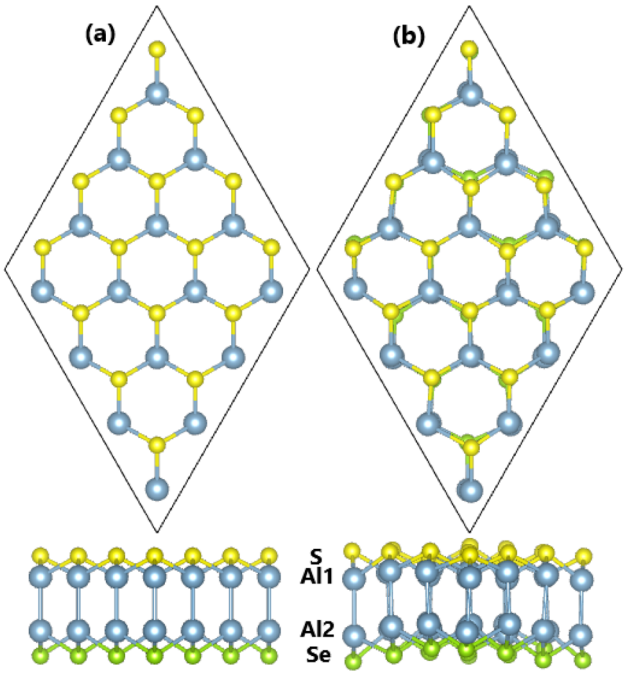

Fig. 1 Visualization of a 4 × 4 × 1 supercell of Janus monolayer Al_2SSe: (a) at equilibrium and (b) after 5 ps of AIMD simulations.

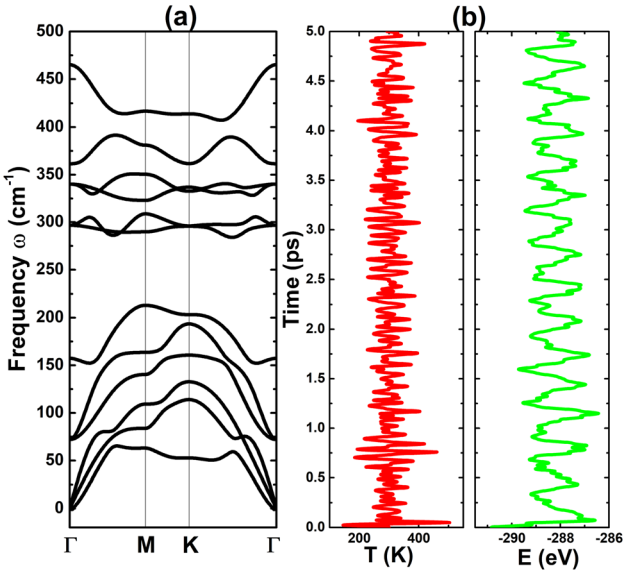

Fig. 2 (a) Phonon dispersion curves and (b) fluctuation of T-temperature and E-energy during AIMD simulations of Janus monolayer Al_2SSe monolayer.

and Al2 refer to aluminum atoms bound to S and Se atoms, respectively. It can be seen the honeycomb arrangement from top-view, where S/Se and Al1/Al2 pairs are vertically aligned. At equilibrium, the structure of Al_2SSe monolayer is characterized by following parameters: (1) lattice constant $a = 3.68$ Å that is in good agreement with previous studies;[48] (2) chemical bond lengths $d_{Al1-S} = 2.36$ Å, $d_{Al1-Al2} = 2.59$ Å, and $d_{Al2-Se} = 2.44$ Å; (3) the monolayer thickness $\Delta_m = \Delta_{Al1-S} + \Delta_{Al1-Al2} + \Delta_{Al2-Se} = 1.02 + 2.59 + 1.21 = 4.82$ Å; and (4) interatomic angles $\angle SAl1S = 102.66°$ and $\angle SeAl2Se = 97.60°$. Then, the stability of Al_2SSe monolayer is tested through phonon dispersion, *ab initio* molecular dynamics (AIMD) simulations, and elastic constants as follow:

• Phonon spectra are calculated within the framework of finite displacement method implemented in PHONOPY code.[65] Results plotted in Fig. 2a show that in the entire Brillouin zone, all the vibrational modes are real. The absence of imaginary modes confirms that Al_2SSe Janus monolayer is dynamically stable.

• AIMD simulations are performed in the canonical ensemble (NVT) along with Nose–Hoover thermostat.[66,67] Herein, a 4 × 4 × 1 supercell is used and total simulation time is set to 5 ps (each time step of 2 fs for 2500 simulation steps) at 300 K. From the final structure visualized in Fig. 1b, no significant migration of the constituent atoms is noted, such that the structure network is well maintained. In addition, the fluctuations of temperature and system energy are found stable during the simulations as observed in Fig. 2b. Based on AIMD simulations, it is safe to conclude that Al_2SSe Janus monolayer has good thermal stability.

• Elastic constants C_{11} and C_{12} of Al_2SSe monolayer are calculated to be 78.965 and 19.579 N m^{-1}, respectively. These values satisfy the criteria of mechanical stability[68] $C_{11} > 0$ and $C_{11} > |C_{12}|$, such that one can safely conclude that Al_2SSe Janus monolayer is mechanically stable.

The electronic nature of Al_2SSe Janus monolayer is studied by calculating its atom- and orbital-decomposed band structure. From Fig. 3a, it can be noted the indirect-gap semiconductor, where the forbidden energy region is found between the highest point of valence band along ΓM path at lowest point of conduction band at M point. Based on our simulations, a band gap of 2.04 eV is obtained for the considered 2D material, which is agreement with previous calculations.[49] The upper part of valence band is formed mainly by chalcogen S and Se atoms, while the lower part of conduction band is originated mainly from S and Al1 atoms. More details can be obtained from the orbital-decomposed band structures given in Fig. S1 of the SI. Specifically, the energy gap is determined mainly by Al1-s, S-p_z, and Se-p_z states. Moreover, $p_{x,y,z}$ states of S and Se atoms build mainly the lower parts of valence band, indicating their occupancy. To further characterize the nature of chemical bonds, electron localization function of Al_2SSe monolayer is illustrated in Fig. 3b. High electron localization at S and Se atoms indicates that Al1–S and Al2–Se chemical bonds are predominantly ionic that is a result of the charge transfer from Al atoms to chalcogen atoms. Our Bader charge analysis asserts that S and Se atoms attract charge quantities of 1.49 and 1.40 e, respectively. Meanwhile the interactions between Al1 and Al2 atoms are mainly covalent as suggested by the charge accumulation between them.

B. Effects of pair Al vacancies

In this part, the effects of pair vertically aligned Al vacancies on the electronic and magnetic properties of Al_2SSe monolayer are investigated. According to our simulations, formation energy of pVa@mo system is calculated to be 3.05 eV per atom that

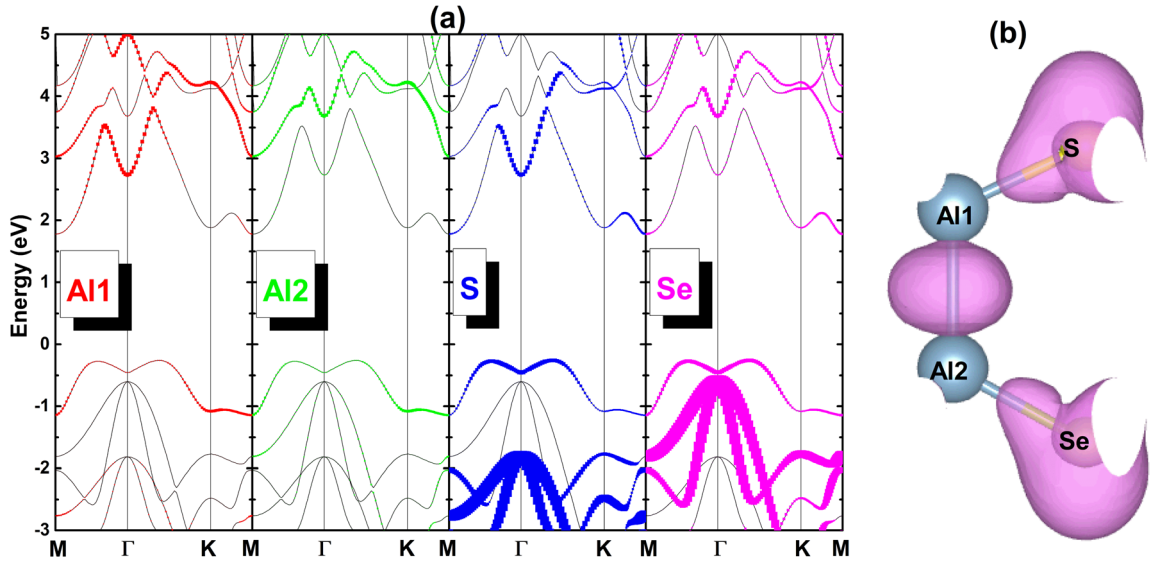

Fig. 3 (a) Atom-decomposed band structure (the Fermi level is set to 0 eV) and (b) electronic localization function (iso-surface value: 0.8 e Å^{-3}) of Janus monolayer Al_2SSe.

indicates the energy required to create pVa-type defect in Al_2SSe monolayer. Then, a negative E_c value of −4.06 eV per atom suggests good structural-chemical stability of this defective system. Based on our spin-polarized calculations, pVa@mo system has a total magnetic moment of 2.00 μ_B, indicating that Al_2SSe monolayer is significantly magnetized by vacancies. Fig. 4 illustrates the spin density in pVa@mo system, which demonstrates that the magnetism is originated primarily from the first neighboring Se and second neighboring Al atoms from defect sites considering large spin iso-surfaces centered at/between them. In this case, S atoms closest to vacancies also make little contribution to the system magnetism. In addition, a negative MAE value of −510.33 μeV is obtained for pVa@mo system, indicating its in-plane magnetic anisotropy (IMA). Such that, the creation of pair Al vacancies may functionalize Al_2SSe monolayer for magnetic field sensing.

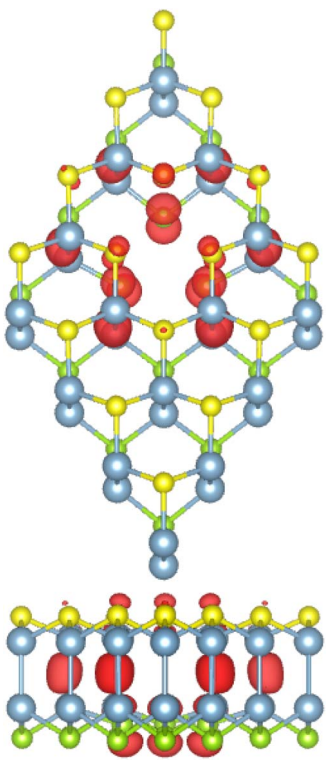

Fig. 4 Spin density (iso-surface value: 0.01 e Å^{-3}; green iso-surface: negative spin value; red iso-surface: positive spin value) distributed in pVa@mo system.

Fig. 5a shows the spin-resolved electronic band structure of pVa@mo system, where the half-metallicity is composed of a metallic spin-up state and a semiconductor spin-down state, suggesting its promise for spintronic applications. In this case, a spin-down band gap of 0.14 eV is obtained. In addition, projected density of states (PDOS) spectra of the first S/Se and second Al1/Al2 neighboring atoms are also given in Fig. 5b to provide more insights into the origin of the half-metallicity. Note that Se-p_z state is the main responsible of the spin-up metallic character, where S-p_z, Al1-p_z, and Al2-p_z states also make smaller contribution to the spin-up mid-gap subband. Meanwhile, the spin-down energy gap is regulated by the separation between Se-$p_{x,y}$ states and Se-p_z/S-p_z/Al1-p_z/Al2-p_z states. From the spin polarization in PDOS spectra, one can safely conclude that p_z state of the mentioned atoms produces mainly magnetic properties of pVa@mo system.

C. Effects of pair transition metal impurities

Herein, the effects of replacing pair vertically aligned Al atoms in Al_2SSe Janus monolayer by pair TM atoms are investigated. TM atoms bound to S and Se atoms are denoted by TM1 and TM2, respectively. Firstly, the magnetic phase is determined by considering the ferromagnetism (FM, in which two TM atoms show parallel spin orientation) and ferrimagnetic (FiM, in which two TM atoms show antiparallel spin orientation), which are visualized in Fig. 6. Based on our simulations, the FiM phase

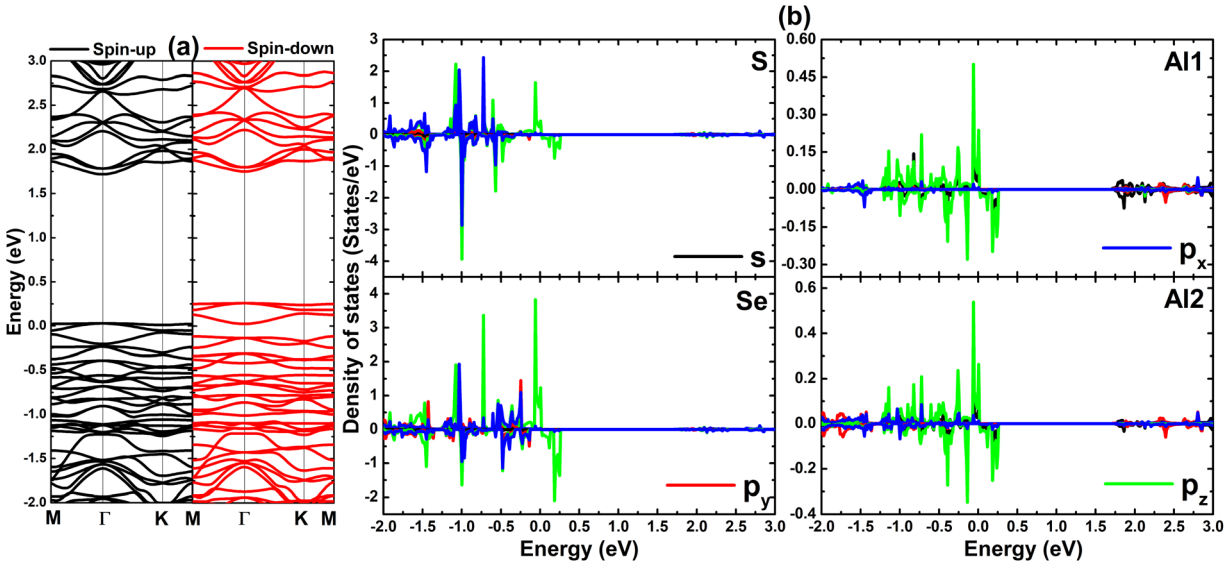

Fig. 5 (a) Spin-resolved band structure and (b) projected density of states of atoms closest to the vacancy sites of pVa@mo system (the Fermi level is set to 0 eV).

is stable in pMn@mo system with an energy of 1121.17 meV smaller than that of FM phase. In contrast, pFe@mo system is intrinsically ferromagnetic with an energy difference of 251.26 meV between magnetic phases. From now on, the stable systems are denoted by FiM-pM@mo and FM-pFe@mo, whose formation energy is calculated to be 2.36 and 1.97 eV per atom, respectively. Note that pTM doping requires less energy than creating pVa vacancies. Moreover, higher energy should be supplied to realize the pMn doping, considering larger E_f value of FiM-pMn@mo system. For ferromagnetic system, Curie temperature T_C is an essential parameter. Therefore, we calculate this parameter of FM-pFe@mo system using the mean-field approximation (MFA) as follows:[69]

$$T_C = \frac{-2\Delta E}{3Nk_B} \quad (4)$$

where ΔE is the energy difference between FM and FiM states; k_B is Boltzmann constant; and $N = 2$ denotes number of transition metals in the supercell. Our calculations provide a high Curie temperature of 972.40 K, suggesting the robustness of the ferromagnetism in FM-pFe@mo system against variation of temperature. It is important mentioning that mean-field approximation overestimates Curie temperature because of the inaccurate description of percolation effects. Therefore, an empirical relation has been proposed to obtain more reliable results:[70] $T_C^{empirical} = 0.51 \times T_C^{MFA}$. According to this relation, an empirical Curie temperature of 495.92 K is obtained, which is above room temperature to suggest promise of the ferromagnetism for practical applications. In addition, the IMA is found in FiM-pMn@mo system as suggested by negative MAE value of −46.16 μeV, meanwhile positive MAE value of 2361.54 μeV confirms the perpendicular magnetic anisotropy (PMA) of FM-pFe@mo system. Such that we can recommend FM-pFe@mo system to fabricate magnetoresistive random-access memories

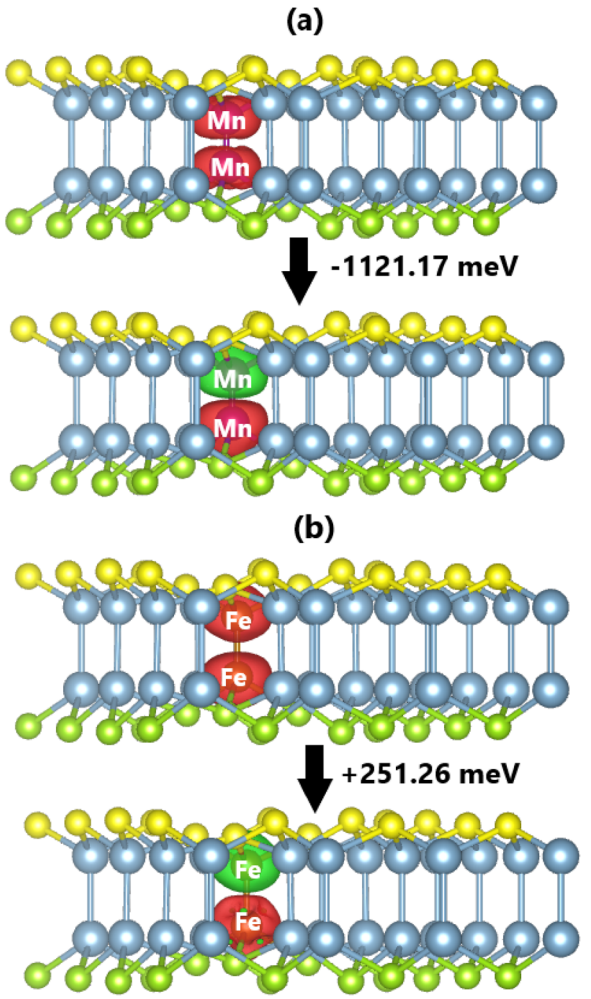

Fig. 6 Spin density (iso-surface value: 0.01 e Å^{-3}; green iso-surface: negative spin value; red iso-surface: positive spin value) and energy of magnetic phase transition of (a) pMn@mo and (b) pFe@mo systems.

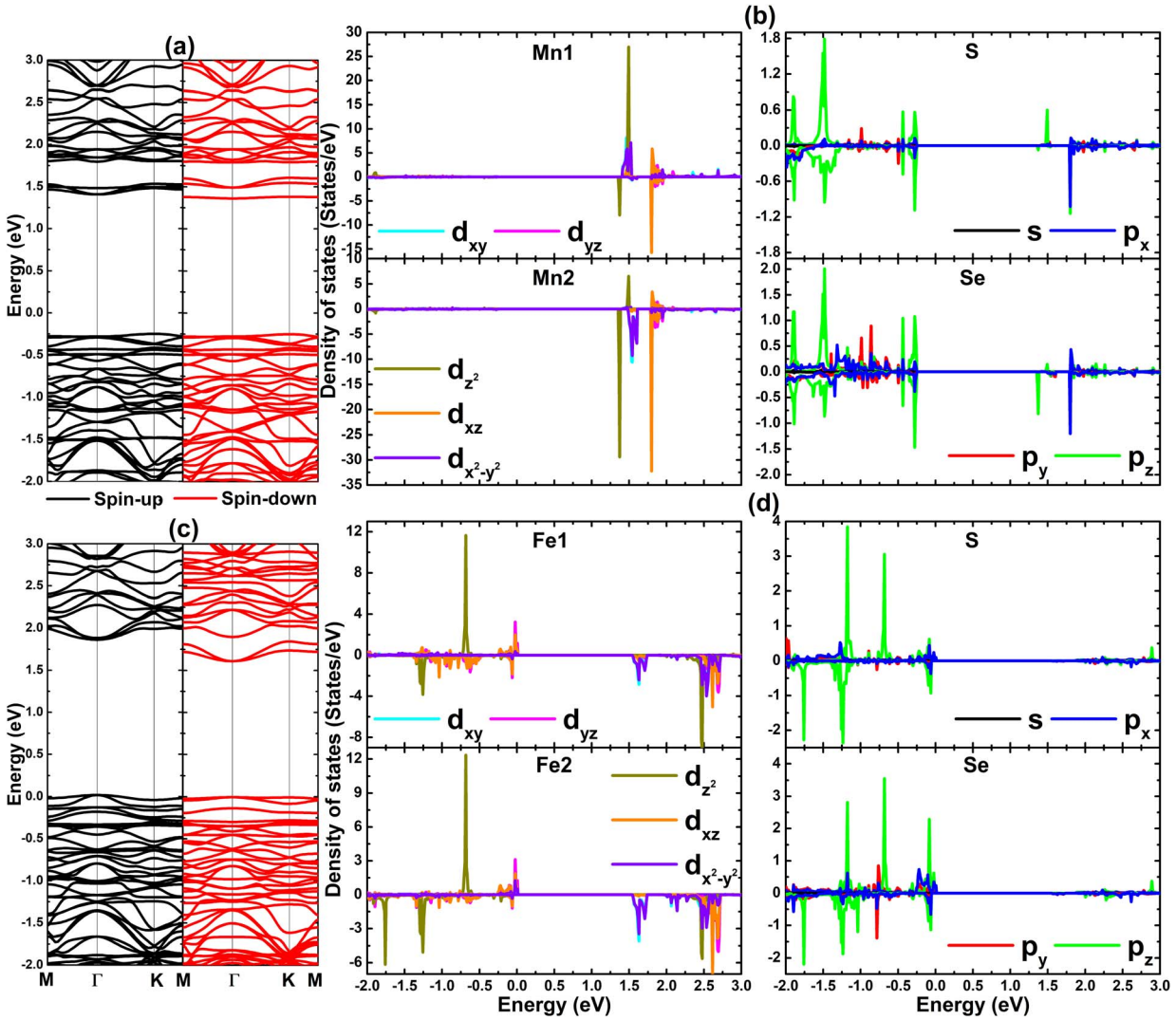

Fig. 7 Spin-resolved band structure and projected density of states of transition metal impurities and their nearest neighboring S/Se atoms of (a and b) pMn@mo and (c and d) pFe@mo systems (the Fermi level is set to 0 eV).

(MRAMs), while FiM-pFe@mo systems shows prospective applicability for the magnetic field sensing.

The spin-resolved band structures of the doped systems are given in Fig. 7a and c. Results demonstrate that pair Mn impurities induce the magnetic semiconductor nature in Al_2SSe Janus monolayer, where both spin-up and spin-down states show the semiconductor character with energy gaps of 1.66 and 1.61 eV, respectively. Otherwise, the half-metallicity is achieved by doping with pair Fe impurities, where the band structure is composed of metallic spin-up state and semiconductor spin-down state with energy gap of 1.6 eV. The emergence of feature-rich properties suggests the pTM doping as effective methods to functionalize Al_2SSe Janus monolayer towards spintronic applications. The contribution of TM impurities and their nearest neighboring S/Se atoms to the pTM@mo systems electronic and magnetic properties is analyzed through their PDOS spectra given in Fig. 7b and d. It can be seen that TM-d_{z^2}–d_{xz} states form mainly the mid-gap subbands above the Fermi level. Moreover, the spin-up metallic character of FM-pFe@mo system is given primarily by Fe-d_{yz} state that hybridizes with Se-p_z state. To study quantitatively the interactions between TM impurities and the host Al_2SSe monolayer, Bader charge analysis is performed. It is found that Mn1/Fe1 and Mn2/Fe2 atoms lose charge quantities of 0.89/0.64 and 0.73/0.53 *e*, respectively. Note that TM1 atoms lose larger charge quantity than TM2 atoms, which is due to that TM1 atoms are surrounded by S atoms that are more electronegative than Se atom (surrounding TM2 atoms). Consequently, pair Mn and Fe impurities transfer charge quantities of 1.53 and 1.26 *e* to the host monolayer, respectively.

D. Effects of hole and electron doping on the defective and doped system

Now, hole and electron doping is proposed to tune the electronic and magnetic properties of 2D defective and doped Al_2SSe systems. For such goal, 0.5 and 1.0 carrier/supercell concentrations is added in 4 × 4 × 1 supercell. Herein, hole concentrations are denoted by negative values, meanwhile positive values refer to the electron concentrations. The carrier-

Table 1 Energy of magnetic phase transition ΔE (meV), magnetic anisotropy energy MAE (μeV), and spin-dependent band gap E_g (eV; spin-up/spin-down) of the defective and doped Al_2SSe systems

	Carrier concentration				
	−1.0	−0.5	0.0	0.5	1.0
pVa@mo					
MAE	0.00	−208.59	−510.33	−803.89	−1147.55
E_g	M/M	M/M	M/0.14	1.66/0.16	1.62/0.17
pMn@mo					
ΔE	1116.15	1119.78	1121.17	805.19	307.42
MAE	111.51	3.26	−46.16	−223.90	1350.79
E_g	M/1.63	1.66/1.61	1.66/1.61	M/1.82	M/1.90
pFe@mo					
ΔE	−270.32	−262.17	−251.26	−542.74	−1535.22
MAE	363.03	215.87	2361.54	2086.64	−1047.95
E_g	1.98/M	M/1.94	M/1.61	M/1.62	1.59/1.56

dependent results of energy of magnetic phase, magnetic anisotropy, and band gap of pVa@mo, pMn@mo, and pFe@mo systems are summarized in Table 1, which are also plotted in Fig. 8.

For the defective pVa@mo system, it is found that electron doping strengthens the monolayer magnetism by increasing overall magnetic moment, meanwhile the magnetization becomes weaker by hole doping and nearly disappears at high hole level. Specifically, total magnetic moments of 0.05, 1.24, 2.45, and 2.97 are obtained at carrier concentrations of −1.0, −0.5, 0.0, 0.5, and 1.0 carrier/supercell, respectively. It is found also that carrier doping preserves the IMA of pVa@mo system, however this is weakened with hole doping considering that MAE values becomes less negative. In contrast, the IMA is considerably strengthened with additional electrons in the system due to that MAE values becomes much more negative (a value of −1147.55 μeV is obtained at 1.0 electron per supercell). Related to the electronic properties, pVa@mo system is metallized by hole doping since both spin states exhibit metallic character, while the transition from half-metallic to magnetic semiconductor nature is induced by electron doping. From these results, it can be safely concluded that electron doping is efficient to enhance the electronic and magnetic properties of pVa@mo system, making it more suitable for spintronic applications.

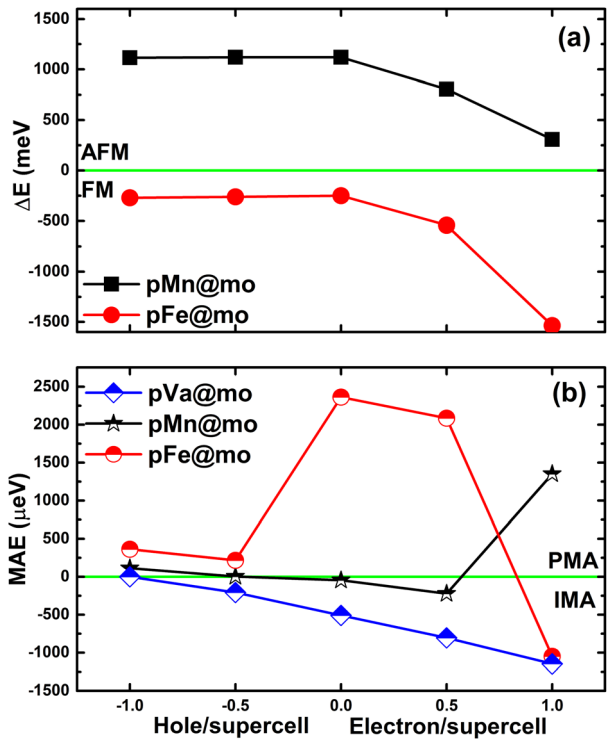

Fig. 8 (a) Energy of magnetic phase transition and (b) magnetic anisotropy energy of pVa@mo, pMn@mo, and pFe@mo systems at difference hole and electron concentrations.

In the cases of pMn-doped Al_2SSe systems, it is found that hole doping influences insignificantly on the energy of magnetic phase transition ΔE, meanwhile electron doping reduces this parameter. The ferrimagnetism is preserved, however the ΔE reduction asserts that FiM state becomes less stable with electron doping. Moreover, the addition of hole gives place to the IMA-to-PMA switching, meanwhile 0.5 electron per supercell enhances the IMA as suggested by more negative MAE value. Further increasing electron level will turn the magnetic anisotropy to PMA with a large positive MAE value of 1350.79 μeV. The electronic properties of pMn@mo system can be effectively controlled by carrier doping, where the half-metallicity or magnetic semiconductor nature can be obtained depending on the carrier concentration. These results demonstrate the effectiveness of carrier doping to selectively make pMn@mo system promising 2D platforms for magnetic field sensing and MRAMs fabrication.

Hole doping is found to not influence significantly on the FM phase of pFe@mo system considering that ΔE exhibits very small variation. In contrast, the ferromagnetism is considerably enhanced with electron doping, where much more negative ΔE values of −542.74 and −1535.22 meV are obtained at 0.5 and 1.0 electron per supercell, respectively. Note that these values correspond to very high Curie temperatures of 2100.40 and 5941.30 K, respectively. Our calculations show that MAE value becomes less positive, suggesting the reduction of PMA stability, where stronger effects are induced by hole doping. At high electron level of 1.0 electron per supercell, the IMA is turned on in pFe-doped Al_2SSe system. In addition, pFe@mo system maintains its half-metallicity with carrier doping, except for 1.0 electron per supercell at which the magnetic semiconductor nature with spin-up/spin-down gaps of 1.59/1.56 eV is obtained. Based on our simulations, the magnetism of pFe@mo system can be effectively modified by electron doping to enhance the ferromagnetism and switch the magnetic anisotropy, meanwhile the hole doping exhibits insignificant effects.

IV. Conclusions

In summary, first-principles calculations have been performed to investigate the magnetism engineering in Al_2SSe Janus

monolayer through lattice defects and TM doping, and further modulation of electronic and magnetic properties through hole and electron doping. Pristine Al_2SSe monolayer has good structural stability, showing a relatively large indirect gap that is determined mainly by Al1-s, S-p_z, and Se-p_z states. The Al1–Al2 chemical bond is predominantly covalent, while the ionic character is confirmed for Al1–S and Al2–Se bonds. The creation of pair Al vacancies induces the half-metallicity, where S-p_z, Se-$p_{x,y,z}$, Al1-p_z, and Al2-p_z states originate mainly the electronic subbands around the Fermi level and produce the system magnetism. The magnetism becomes weaker with hole doping, and disappears with high hole level. In contrast, electron doping can strengthen the system magnetism and enhance the in-plane magnetic anisotropy to make pVa@mo system more suitable for magnetic field sensing. Hole doping metallizes pVa@mo system, while the transition from half-metallic to magnetic semiconductor nature is achieved by electron doping. Doping with pair Mn atoms induces the ferrimagnetism with IMA in Al_2SSe monolayer, while the ferromagnetism with PMA is obtained by doping with pair Fe atoms. Moreover, doping approaches make strong spin polarization at the vicinity of the Fermi level, which can be attributed to TM-3d orbital that also originates primarily magnetic properties. Hole doping influences insignificantly on the magnetic state of the doped system. Meanwhile electron doping is found to weaken the FiM state of pMn@mo system and enhance considerably the ferromagnetism of pFe@mo system. Depending on the carrier concentration, magnetic anisotropy can be switched from IMA to PMA, and vice verse. Moreover, feature-rich half-metallic and magnetic semiconductor natures can be also modulated by varying the carrier level. Our results may introduce promising 2D spintronic materials made from Al_2SSe Janus monolayer, where selective applications can be designed by hole and electron doping.

Conflicts of interest

The authors declare that they have no known competing financial interests or personal relationships that could have appeared to influence the work reported in this paper.

Data availability

Data will be provided under requesting to authors.

Supplementary information: orbital-decomposed band structure of Al_2SSe Janus monolayer that provide insights into the contribution to the formation of band structure. See DOI: https://doi.org/10.1039/d5ra09165a.

Acknowledgements

Calculations were performed in DGCTIC-UNAM Supercomputing Center (projects LANCAD-UNAM-DGTIC-368 and LANCAD-UNAM-DGTIC-422).

References

1 N. Baig, I. Kammakakam and W. Falath, Nanomaterials: A review of synthesis methods, properties, recent progress, and challenges, *Mater. Adv.*, 2021, **2**(6), 1821–1871.
2 V. Singh, P. Yadav and V. Mishra, Recent advances on classification, properties, synthesis, and characterization of nanomaterials, *Green Synth. Nanomater. Bioenergy Appl.*, 2020, 83–97.
3 V. Shanmugam, R. A. Mensah, K. Babu, S. Gawusu, A. Chanda, Y. Tu, R. E. Neisiany, M. Försth, G. Sas and O. Das, A review of the synthesis, properties, and applications of 2D materials, *Part. Part. Syst. Charact.*, 2022, **39**(6), 2200031.
4 S. Das, M. Kim, J.-w. Lee and W. Choi, Synthesis, properties, and applications of 2-D materials: A comprehensive review, *Crit. Rev. Solid State Mater. Sci.*, 2014, **39**(4), 231–252.
5 K. S. Novoselov, A. K. Geim, S. V. Morozov, D.-e. Jiang, Y. Zhang, S. V. Dubonos, I. V. Grigorieva and A. A. Firsov, Electric field effect in atomically thin carbon films, *Science*, 2004, **306**(5696), 666–669.
6 J. Wu, H. Lin, D. J. Moss, K. P. Loh and B. Jia, Graphene oxide for photonics, electronics and optoelectronics, *Nat. Rev. Chem.*, 2023, **7**(3), 162–183.
7 B. Sensale-Rodriguez, Graphene-based optoelectronics, *J. Lightwave Technol.*, 2015, **33**(5), 1100–1108.
8 D. A. Brownson, D. K. Kampouris and C. E. Banks, An overview of graphene in energy production and storage applications, *J. Power Sources*, 2011, **196**(11), 4873–4885.
9 M. Ye, Z. Zhang, Y. Zhao and L. Qu, Graphene platforms for smart energy generation and storage, *Joule*, 2018, **2**(2), 245–268.
10 W. Tian, X. Liu and W. Yu, Research progress of gas sensor based on graphene and its derivatives: A review, *Appl. Sci.*, 2018, **8**(7), 1118.
11 K. Toda, R. Furue and S. Hayami, Recent progress in applications of graphene oxide for gas sensing: A review, *Anal. Chim. Acta*, 2015, **878**, 43–53.
12 C. Su and K. P. Loh, Carbocatalysts: graphene oxide and its derivatives, *Acc. Chem. Res.*, 2013, **46**(10), 2275–2285.
13 X. Fan, G. Zhang and F. Zhang, Multiple roles of graphene in heterogeneous catalysis, *Chem. Soc. Rev.*, 2015, **44**(10), 3023–3035.
14 T. M. Magne, T. de Oliveira Vieira, L. M. R. Alencar, F. F. M. Junior, S. Gemini-Piperni, S. V. Carneiro, L. M. Fechine, R. M. Freire, K. Golokhvast, P. Metrangolo, *et al.*, Graphene and its derivatives: understanding the main chemical and medicinal chemistry roles for biomedical applications, *J. Nanostruct. Chem.*, 2022, **12**(5), 693–727.
15 A. N. Banerjee, Graphene and its derivatives as biomedical materials: Future prospects and challenges, *Interface Focus*, 2018, **8**(3), 20170056.
16 A. Jilani, M. H. D. Othman, M. O. Ansari, S. Z. Hussain, A. F. Ismail and I. U. Khan, Inamuddin, Graphene and its derivatives: synthesis, modifications, and applications in

wastewater treatment, *Environ. Chem. Lett.*, 2018, **16**(4), 1301–1323.

17 V. Karthik, P. Selvakumar, P. Senthil Kumar, D.-V. N. Vo, M. Gokulakrishnan, P. Keerthana, V. Tamil Elakkiya and R. Rajeswari, Graphene-based materials for environmental applications: a review, *Environ. Chem. Lett.*, 2021, **19**(5), 3631–3644.

18 C. Huo, Z. Yan, X. Song and H. Zeng, 2D materials via liquid exfoliation: a review on fabrication and applications, *Sci. Bull.*, 2015, **60**(23), 1994–2008.

19 M. Zhao, C. Casiraghi and K. Parvez, Electrochemical exfoliation of 2D materials beyond graphene, *Chem. Soc. Rev.*, 2024, **53**(6), 3036–3064.

20 Z. Cai, B. Liu, X. Zou and H.-M. Cheng, Chemical vapor deposition growth and applications of two-dimensional materials and their heterostructures, *Chem. Rev.*, 2018, **118**(13), 6091–6133.

21 J. Yu, J. Li, W. Zhang and H. Chang, Synthesis of high quality two-dimensional materials via chemical vapor deposition, *Chem. Sci.*, 2015, **6**(12), 6705–6716.

22 S. M. Poh, X. Zhao, S. J. R. Tan, D. Fu, W. Fei, L. Chu, D. Jiadong, W. Zhou, S. J. Pennycook, A. H. Castro Neto, *et al.*, Molecular beam epitaxy of highly crystalline $MoSe_2$ on hexagonal boron nitride, *ACS Nano*, 2018, **12**(8), 7562–7570.

23 R. Yue, A. T. Barton, H. Zhu, A. Azcatl, L. F. Pena, J. Wang, X. Peng, N. Lu, L. Cheng, R. Addou, *et al.*, $HfSe_2$ thin films: 2D transition metal dichalcogenides grown by molecular beam epitaxy, *ACS Nano*, 2015, **9**(1), 474–480.

24 X. Wan, E. Chen, J. Yao, M. Gao, X. Miao, S. Wang, Y. Gu, S. Xiao, R. Zhan, K. Chen, *et al.*, Synthesis and characterization of metallic Janus MoSH monolayer, *ACS Nano*, 2021, **15**(12), 20319–20331.

25 S. Zhao, T. Hotta, T. Koretsune, K. Watanabe, T. Taniguchi, K. Sugawara, T. Takahashi, H. Shinohara and R. Kitaura, Two-dimensional metallic NbS_2: growth, optical identification and transport properties, *2D Mater.*, 2016, **3**(2), 025027.

26 M. A. Kharadi, G. F. A. Malik, F. A. Khanday, K. A. Shah, S. Mittal and B. K. Kaushik, Silicene: From material to device applications, *ECS J. Solid State Sci. Technol.*, 2020, **9**(11), 115031.

27 M. E. Dávila and G. Le Lay, Few layer epitaxial germanene: a novel two-dimensional dirac material, *Sci. Rep.*, 2016, **6**(1), 20714.

28 C. Cong, J. Shang, X. Wu, B. Cao, N. Peimyoo, C. Qiu, L. Sun and T. Yu, Synthesis and optical properties of large-area single-crystalline 2D semiconductor WS_2 monolayer from chemical vapor deposition, *Adv. Opt. Mater.*, 2014, **2**(2), 131–136.

29 Y. Lu and J. H. Warner, Synthesis and applications of wide bandgap 2D layered semiconductors reaching the green and blue wavelengths, *ACS Appl. Electron. Mater.*, 2020, **2**(7), 1777–1814.

30 K. Zhang, Y. Feng, F. Wang, Z. Yang and J. Wang, Two dimensional hexagonal boron nitride (2D-hBN): synthesis, properties and applications, *J. Mater. Chem. C*, 2017, **5**(46), 11992–12022.

31 H. Zhang, M. Holbrook, F. Cheng, H. Nam, M. Liu, C.-R. Pan, D. West, S. Zhang, M.-Y. Chou and C.-K. Shih, Epitaxial growth of two-dimensional insulator monolayer honeycomb BeO, *ACS Nano*, 2021, **15**(2), 2497–2505.

32 L. Kou, Y. Ma, Z. Sun, T. Heine and C. Chen, Two-dimensional topological insulators: Progress and prospects, *J. Phys. Chem. Lett.*, 2017, **8**(8), 1905–1919.

33 Y. Liang, M. Khazaei, A. Ranjbar, M. Arai, S. Yunoki, Y. Kawazoe, H. Weng and Z. Fang, Theoretical prediction of two-dimensional functionalized MXene nitrides as topological insulators, *Phys. Rev. B*, 2017, **96**(19), 195414.

34 A. Mancini, G. Micocci and A. Rizzo, New materials for optoelectronic devices: Growth and characterization of indium and gallium chalcogenide layer compounds, *Mater. Chem. Phys.*, 1983, **9**(1–3), 29–54.

35 M. Afzaal and P. O'Brien, Recent developments in II–VI and III–VI semiconductors and their applications in solar cells, *J. Mater. Chem.*, 2006, **16**(17), 1597–1602.

36 T. Tanabe, K. Suto, J.-i. Nishizawa and T. Sasaki, Characteristics of terahertz-wave generation from GaSe crystals, *J. Phys. D: Appl. Phys.*, 2003, **37**(2), 155.

37 K. Allakhverdiev, M. Yetis, S. Özbek, T. Baykara and E. Y. Salaev, Effective nonlinear GaSe crystal. optical properties and applications, *Laser Phys.*, 2009, **19**(5), 1092–1104.

38 Z. Yang and J. Hao, Recent progress in 2D layered III–VI semiconductors and their heterostructures for optoelectronic device applications, *Adv. Mater. Technol.*, 2019, **4**(8), 1900108.

39 K. Xu, L. Yin, Y. Huang, T. A. Shifa, J. Chu, F. Wang, R. Cheng, Z. Wang and J. He, Synthesis, properties and applications of 2D layered $M^{III}X^{VI}$ (M= Ga, In; X= S, Se, Te) materials, *Nanoscale*, 2016, **8**(38), 16802–16818.

40 D. Hoat, N. T. Tien, D. K. Nguyen and J. Guerrero-Sanchez, Antiferromagnetism in GaS monolayer doped with TM–TM atom pairs (TM= V, Cr, Mn, and Fe), *Phys. Chem. Chem. Phys.*, 2024, **26**(27), 18657–18666.

41 P. T. Bui, V. Van On, J. Guerrero-Sanchez and D. Hoat, A systematic study of GaSe monolayer doped/codoped with transition metals (Mn and Fe) and pnictogen atoms (P and As), *J. Magn. Magn. Mater.*, 2025, **621**, 172920.

42 D. Wang, X.-B. Li and H.-B. Sun, Native defects and substitutional impurities in two-dimensional monolayer InSe, *Nanoscale*, 2017, **9**(32), 11619–11624.

43 D. G. Hopkinson, V. Zólyomi, A. P. Rooney, N. Clark, D. J. Terry, M. Hamer, D. J. Lewis, C. S. Allen, A. I. Kirkland, Y. Andreev, *et al.*, Formation and healing of defects in atomically thin GaSe and InSe, *ACS Nano*, 2019, **13**(5), 5112–5123.

44 R. Meng, M. Houssa, K. Iordanidou, G. Pourtois, V. Afanasiev and A. Stesmans, Ferromagnetism and half-metallicity in two-dimensional MO (M= Ga, In) monolayers induced by hole doping, *Phys. Rev. Mater.*, 2020, **4**(7), 074001.

45 M.-Y. Liu, Y. He, Y. Mao and K. Xiong, High-temperature ferromagnetism and half-metallicity in hole-doped Janus

OM_2S (M= Ga, In, and Tl) monolayers, *Phys. Rev. B: Condens. Matter Mater. Phys.*, 2022, **105**(3), 035418.
46 X. Chen, Y. Huang, J. Liu, H. Yuan and H. Chen, Thermoelectric performance of two-dimensional AlX (X= S, Se, Te): A first-principles-based transport study, *ACS Omega*, 2019, **4**(18), 17773–17781.
47 G. S. Khosa, S. Kumar, S. Gupta and R. Kumar, Effect of biaxial strain on the electronic structure and transport properties of AlX (X= S or Se) monolayer, *Pramana*, 2022, **96**(3), 124.
48 G. S. Khosa, S. Gupta and R. Kumar, First-principles investigations of electronic and thermoelectric properties of Janus Al_2SSe monolayer, *Phys. B*, 2021, **615**, 413057.
49 C. Q. Nguyen, N. V. Hieu, H. V. Phuc, C. V. Nguyen, N. N. Hieu, T. V. Vu, H. T. Nguyen, *et al.*, Theoretical insights into tunable electronic and optical properties of Janus Al_2SSe monolayer through strain and electric field, *Optik*, 2021, **238**, 166761.
50 G. Guo, Y. Zhou, G. Guo and Z. Xie, First-principles study on the optoelectronic and photocatalytic properties of the C2h-Janus Al_2XY (X/Y = S, Se and Te) monolayers, *Mater. Today Chem.*, 2024, **35**, 101913.
51 M. Demirtas, M. J. Varjovi, M. M. Çiçek and E. Durgun, Tuning structural and electronic properties of two-dimensional aluminum monochalcogenides: Prediction of Janus Al_2XX' (X/X': O, S, Se, Te) monolayers, *Phys. Rev. Mater.*, 2020, **4**(11), 114003.
52 D. Shen, B. Zhao, Z. Zhang, H. Zhang, X. Yang, Z. Huang, B. Li, R. Song, Y. Jin, R. Wu, *et al.*, Synthesis of group VIII magnetic transition-metal-doped monolayer $MoSe_2$, *ACS Nano*, 2022, **16**(7), 10623–10631.
53 H.-P. Komsa, J. Kotakoski, S. Kurasch, O. Lehtinen, U. Kaiser and A. V. Krasheninnikov, Two-dimensional transition metal dichalcogenides under electron irradiation: Defect production and doping, *Phys. Rev. Lett.*, 2012, **109**(3), 035503.
54 W. Kohn and L. J. Sham, Self-consistent equations including exchange and correlation effects, *Phys. Rev.*, 1965, **140**(4A), A1133.
55 J. P. Perdew, K. Burke and M. Ernzerhof, Generalized gradient approximation made simple, *Phys. Rev. Lett.*, 1996, **77**(18), 3865.
56 S. Adhikari, J. Clary, R. Sundararaman, C. Musgrave, D. Vigil-Fowler and C. Sutton, Accurate prediction of HSE06 band structures for a diverse set of materials using δ-learning, *Chem. Mater.*, 2023, **35**(20), 8397–8405.
57 R. Shinde, S. S. Yamijala and B. M. Wong, Improved band gaps and structural properties from Wannier–Fermi–löwdin self-interaction corrections for periodic systems, *J. Phys.: Condens. Matter*, 2020, **33**(11), 115501.
58 B. G. Janesko, Replacing hybrid density functional theory: motivation and recent advances, *Chem. Soc. Rev.*, 2021, **50**(15), 8470–8495.
59 G. Kresse and J. Furthmüller, Efficiency of ab-initio total energy calculations for metals and semiconductors using a plane-wave basis set, *Comput. Mater. Sci.*, 1996, **6**(1), 15–50.
60 G. Kresse and J. Furthmüller, Efficient iterative schemes for ab initio total-energy calculations using a plane-wave basis set, *Phys. Rev. B: Condens. Matter Mater. Phys.*, 1996, **54**(16), 11169.
61 S. L. Dudarev, G. A. Botton, S. Y. Savrasov, C. Humphreys and A. P. Sutton, Electron-energy-loss spectra and the structural stability of nickel oxide: An LSDA+U study, *Phys. Rev. B: Condens. Matter Mater. Phys.*, 1998, **57**(3), 1505.
62 M. Wu, X. Yao, Y. Hao, H. Dong, Y. Cheng, H. Liu, F. Lu, W. Wang, K. Cho and W.-H. Wang, Electronic structures, magnetic properties and band alignments of 3d transition metal atoms doped monolayer MoS_2, *Phys. Lett. A*, 2018, **382**(2–3), 111–115.
63 S. Grimme, J. Antony, S. Ehrlich and H. Krieg, A consistent and accurate ab initio parametrization of density functional dispersion correction (DFT-D) for the 94 elements H-Pu, *J. Chem. Phys.*, 2010, **132**(15), 154104.
64 H. J. Monkhorst and J. D. Pack, Special points for Brillouin-zone integrations, *Phys. Rev. B*, 1976, **13**(12), 5188.
65 A. Togo, L. Chaput, T. Tadano and I. Tanaka, Implementation strategies in phonopy and phono3py, *J. Phys.: Condens. Matter*, 2023, **35**(35), 353001, DOI: 10.1088/1361-648X/acd831.
66 S. Nosé, A unified formulation of the constant temperature molecular dynamics methods, *J. Chem. Phys.*, 1984, **81**(1), 511–519.
67 W. G. Hoover, Canonical dynamics: Equilibrium phase-space distributions, *Phys. Rev. A*, 1985, **31**(3), 1695.
68 F. Mouhat and F.-X. Coudert, Necessary and sufficient elastic stability conditions in various crystal systems, *Phys. Rev. B: Condens. Matter Mater. Phys.*, 2014, **90**(22), 224104.
69 J. Kudrnovsky, I. Turek, V. Drchal, F. Máca, P. Weinberger and P. Bruno, Exchange interactions in III-V and group-IV diluted magnetic semiconductors, *Phys. Rev. B: Condens. Matter Mater. Phys.*, 2004, **69**(11), 115208.
70 Z. Liu, J. Liu and J. Zhao, YN_2 monolayer: Novel p-state Dirac half metal for high-speed spintronics, *Nano Res.*, 2017, **10**(6), 1972–1979.